


Low-Noise and Linear Nonmagnetic Circulator by a Temporal Nonreciprocal Phase Shifter

Sajjad Taravati¹* and George V. Eleftheriades

The Edward S. Rogers Sr. Department of Electrical and Computer Engineering, University of Toronto, Toronto, Ontario M5S 3H7, Canada

 (Received 12 April 2022; revised 12 August 2022; accepted 22 August 2022; published 29 September 2022)

Conventional circulators are made of magnetic ferrites and suffer from a cumbersome architecture, incompatibility with integrated circuit technology, and inability for high-frequency applications. To overcome these limitations, here we propose a low-noise, lightweight, low-profile, and linear nonmagnetic circulator comprising a nonreciprocal time-varying phase shifter. This circulator is composed of a nonreciprocal temporal phase shifter and two reciprocal delay-line-based phase shifters. The proposed nonreciprocal temporal phase shifter is based on the generation of time-harmonic signals, enforcing destructive interference for undesired time harmonics and constructive interference for desired time harmonics at different locations of the structure. Such a unique task is accomplished through two phase-engineered temporal loops. The phase and frequency of these two loops are governed by external signals with different phases, imparting an effective electronic angular momentum to the system. We observe a large isolation level of greater than 32.3 dB, a low noise figure of less than 2.5 dB, a P1dB of +30.2 dBm, and IIP3 of +43.5 dBm. Furthermore, this circulator is endowed with a reconfigurable architecture and can be directly embedded in a conventional integrated circuit (IC) technology to realize a class of high-power handling and linear IC circulators.

DOI: [10.1103/PhysRevApplied.18.034082](https://doi.org/10.1103/PhysRevApplied.18.034082)

I. INTRODUCTION

Circulators are three-port nonreciprocal devices and represent key elements for full-duplex telecommunication transceivers [1–6]. They are used to separate the transmitter and receiver paths by introducing nonreciprocity between their ports [4,7]. Conventional circulators are formed by ferrite magnetic materials, where nonreciprocity is achieved under a magnetic bias field [3,8,9]. However, ferrite-based magnetic circulators are bulky, costly, heavy and are not available at high frequencies. Recently, nonmagnetic nonreciprocity has spurred a surge of research activity to eliminate the issues associated with magnetic nonreciprocal devices.

Nonmagnetic nonreciprocity is conventionally achieved through nonreciprocal properties of transistors at microwave frequencies [10–16], and electro-optical modulators at optical frequencies [17]. However, these techniques substitute the absence of cumbersome magnetic bias for other tangible drawbacks, such as poor noise performance and strong nonlinearities of transistors, or the complexity and large size of the electro-optical modulators. Recently, space-time modulation has been shown to be a remarkable approach to realize nonreciprocal components, especially

for integrated optical networks where they can be fully realized using silicon photonics [18–20]. It is shown that by taking advantage of one-way progressive wave coupling in a space-time-modulated structure, nonreciprocal devices and isolators can be created [18,21–26]. The space-time modulation technique exhibits appealing capabilities, such as parametric wave amplification [27–29], unidirectional beam splitting [30], pure frequency generation [31,32], nonreciprocal metasurfaces [33–36], antennas [37], nonreciprocal filters [38], and full-transceiver realization [39,40].

Nevertheless, the space-time modulation technique requires optically long structures as they rely on the weak and progressive wave coupling, acousto-optic and electro-optic effects [21,22,34,41,42]. Time-varying circulators [19,43–47] have shown to be a good candidate to realize versatile nonmagnetic wave circulators. They offer outstanding noise performance, and are compatible with integrated circuit technology and high-frequency applications. Additionally, phase-engineered time modulation has recently been considered as an alternative approach to realize unique functionalities and devices [37,48]. Phase-engineered time-modulated structure provides a low-profile and efficient platform for wave engineering by taking advantage of asymmetric frequency-phase transitions.

*sajjad.taravati@utoronto.ca

Within this context, this study proposes a low-profile, lightweight, and nonmagnetic circulator based on a nonreciprocal phase shifter at microwaves. This nonreciprocal phase shifter is constituted of two time-modulated loops, each of which comprising phase-engineered temporal transmission lines. The lightweight and low-profile properties originate from the fact that the time modulation requires only four temporal varactors. Isolation between different ports is achieved by imposing specified constructive and destructive interferences at the ports of the circulator. We show that by proper design of the band structure of the phase-engineered temporal transmission lines, a desired nonreciprocal phase shift and consequently, strong signal isolation between the three ports of the circulator can be achieved. The frequency and phase transition in a time-varying transmission line are provided by varactors biased by a time-varying voltage. The circulator exhibits strong isolation of more than 32.3 dB, highly linear response, that is, 1-dB compression point of 30.2 dBm, broad-band operation where more than 20-dB isolation is introduced across a 22% fractional bandwidth. This circulator can be realized using integrated circuit (IC) technology for a much smaller dimension and programmable mechanism.

II. RESULTS

A. Circulator design

Figure 1 depicts the architecture of the proposed time-modulated circulator. The circulator is composed of a nonreciprocal time-varying phase shifter between ports 1 and 2, and two reciprocal phase shifters (e.g., transmission lines) between ports 1 and 3 and between ports 2 and 3. To compute the required phase shifts at the three arms of

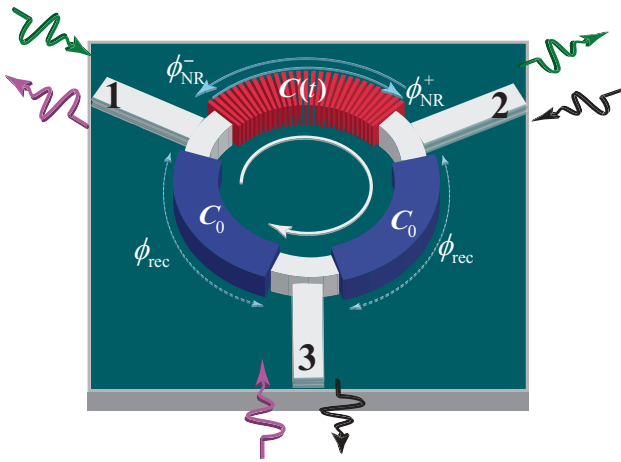


FIG. 1. Schematic illustration of the time-modulated circulator composed of a nonreciprocal time-varying phase shifter and two reciprocal phase shifters.

the circulator, we excite a given port and ensure constructive interference at the next right-side port, and destructive interference at the next left-side port. For instance, we first excite port 1. Then, a full transmission (constructive interference) from port 1 to port 2 requires

$$\phi_{\text{NR}}^+ = 2\phi_{\text{rec}}, \quad (1a)$$

whereas a null (destructive interference) at port 3 may be achieved by satisfying

$$\phi_{\text{rec}} = \phi_{\text{NR}}^+ + \phi_{\text{rec}} - \pi, \quad (1b)$$

where ϕ_{NR}^+ is the forward phase shift of the nonreciprocal phase shifter, from left to right, and ϕ_{rec} is the phase shift provided by reciprocal phase shifters. Next, we excite port 2, where a full transmission (constructive interference) from port 2 to port 3 requires

$$\phi_{\text{rec}} = \phi_{\text{NR}}^- + \phi_{\text{rec}}, \quad (1c)$$

where ϕ_{NR}^- denotes the backward phase shift of the nonreciprocal phase shifter, from right to left. A null (destructive interference) at port 1 can be satisfied by

$$\phi_{\text{NR}}^- = 2\phi_{\text{rec}} - \pi. \quad (1d)$$

Hence, by setting $\phi_{\text{rec}} = \pi/2$, $\phi_{\text{NR}}^+ = \pi$, and $\phi_{\text{NR}}^- = 0$, the desired constructive and destructive interferences between three ports of the circulator in Fig. 1 can be achieved.

The two reciprocal phase shifters may be realized by lumped elements at low frequencies or using transmission lines at high frequencies. The nonreciprocal phase shifter is realized by a time-varying lightweight and highly efficient phase shifter, where the effective electric permittivity of a transmission line is time modulated.

B. Temporal nonreciprocal phase shifter

Figure 2 depicts the architecture of the temporal nonreciprocal phase shifter, formed by two time-varying loops, each of which is composed of two phase-engineered temporal transmission lines. The left temporal loop is composed of two (upper and lower) temporal transmission lines, where the capacitance of the transmission lines is modulated in time considering a π phase difference between the lower Fig. (2a) and upper Fig. (2b) temporal transmission lines, i.e.,

$$C_1(t) = C_{\text{av}} + \delta \cos(\Omega t), \quad (2a)$$

$$C'_1(t) = C_{\text{av}} + \delta \cos(\Omega t + \pi), \quad (2b)$$

where C_{av} is the average capacitance of the loops and δ is the modulation amplitude of the loops. In addition, Ω

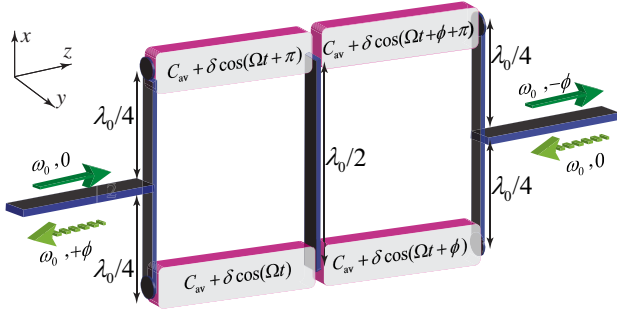


FIG. 2. Schematic representation of the nonreciprocal phase shifter integrating two time-modulated loops.

denotes the temporal modulation frequency. The right temporal loop is composed of two (upper and lower) temporal transmission lines, where the capacitance of the transmission lines is modulated in time considering a π -phase difference between the upper and lower temporal transmission lines and ϕ -phase difference with the left loop, i.e.,

$$C_2(t) = C_{av} + \delta \cos(\Omega t + \phi), \quad (2c)$$

$$C'_2(t) = C_{av} + \delta \cos(\Omega t + \phi + \pi), \quad (2d)$$

where ϕ represents the modulation phase difference between the first and second loops. Next, by proper design of the time modulation of the two loops, a desired nonreciprocal phase shift is achieved. These two temporal loops are designed to provide appropriate constructive interference for the desired time harmonics and destructive interference for the undesired time harmonics.

Figure 3 shows a schematic representation of the dispersion diagram for asymmetric frequency-phase transitions in a temporal transmission line. Here, a frequency up-conversion from ω_0 to $\omega_0 + \Omega$ is accompanied by a positive additive phase, i.e., $+\phi_1$ in the forward transmission and $+\phi_2$ in the backward transmission. However, a frequency down-conversion from $\omega_0 + \Omega$ to ω_0 is accompanied by a negative additive phase, i.e., $-\phi_2$ in the forward transmission and $-\phi_1$ in the backward transmission.

To best understand the effect of the phase and amplitude of the time modulation on the output voltage of the temporal transmission line, we first investigate the variation of the voltage through a temporal-varactor-loaded transmission line. It may be shown that, by proper engineering of the dispersion of the transmission line, the output voltage acquires a frequency transition (up- or down-conversion) accompanied by a phase transition. We assume the dispersion bands of the structure are engineered so that only the fundamental and the first higher-order time harmonics are excited, whereas all higher-order time harmonics are suppressed. Hence, the voltage is defined based on the superposition of the $n = 0$ and $n = -1$ space-time harmonics fields. Considering a forward wave traveling along

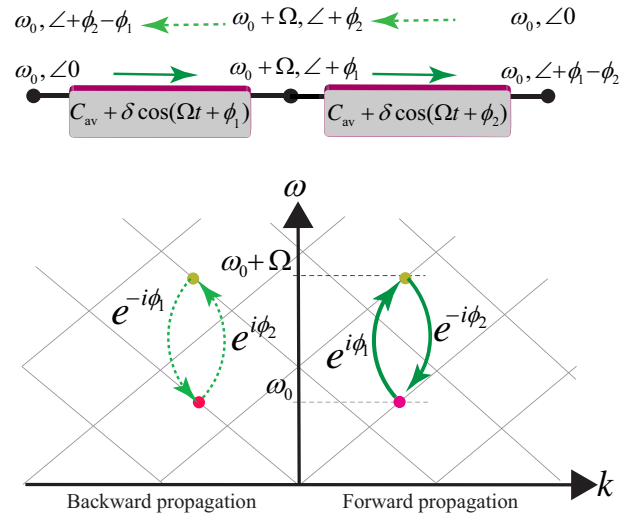


FIG. 3. Schematic representation of forward and backward frequency-phase transitions in two cascaded temporal transmission line.

$+z$ direction, the voltage may be expressed as

$$V_S(z, t) = v_0(z)e^{-i(k_z z - \omega_0 t)} + v_1(z)e^{-i(k_z z - (\omega_0 + \Omega)t)}. \quad (3)$$

Equation (3) considers an identical wave number k_0 for both the fundamental and the higher-order harmonics as the transmission line is modulated only in time, and not in space. It may be seen from Fig. 3 that, as a result of the temporal sinusoidally periodic capacitance, the dispersion diagram of the temporal transmission line is periodic with respect to the ω axis [49], that is $k(\omega_0 + \Omega) = k(\omega_0) = k_0 = \omega_0/v_p$. Here, $v_p = c/\sqrt{\epsilon_{\text{eff}}}$ is the phase velocity of the wave inside the background transmission line, where ϵ_{eff} is the effective permittivity of the transmission line. Such a temporal periodicity leads to vertical electromagnetic transitions in the dispersion diagram, as shown in Fig. 3. The unknown spatially variant amplitudes $v_0(z)$ and $v_1(z)$ are to be found through satisfying both the telegrapher's equations and the initial conditions at $z = 0$. We then consider a lossless transmission line with time-varying capacitance, the telegrapher's equations read

$$\frac{\partial V(z, t)}{\partial z} = -L_0 \frac{\partial I(z, t)}{\partial t}, \quad (4a)$$

$$\frac{\partial I(z, t)}{\partial z} = -C_0 \frac{\partial [C_{\text{eq}}(t)V(z, t)]}{\partial t}, \quad (4b)$$

where L_0 and C_0 are the inductance and capacitance per unit length of the transmission line, respectively. Equations (4a) and (4b) yield

$$\frac{\partial^2 V(z, t)}{\partial z^2} = \frac{1}{v_p^2} \frac{\partial^2 [C_{\text{eq}}(t)V(z, t)]}{\partial t^2}, \quad (5)$$

where $v_p = 1/\sqrt{L_0 C_0}$.

We then insert the voltage in Eq. (3) into Eq. (5) and take the space and time derivatives, while considering a slowly varying envelope approximation, and apply $\int_0^{2\pi/\Omega} dt$ to both sides of the resultant equation, which yields

$$\frac{dv_0(z)}{dz} = \frac{ik_0\delta}{4C_{av}} e^{-i\phi} v_1(z), \quad (6)$$

$$\frac{dv_1(z)}{dz} = \frac{ik_1^2\delta}{4k_z C_{av}} e^{i\phi} v_0(z). \quad (7)$$

Next, we seek independent differential equations for $v_0(z)$ and $v_1(z)$, which yields

$$\frac{d^2 v_0(z)}{dz^2} - \gamma_0 \gamma_1 v_0(z) = 0, \quad (8)$$

$$\frac{d^2 v_1(z)}{dz^2} - \gamma_0 \gamma_1 v_1(z) = 0, \quad (9)$$

which are second-order differential equations, where $\gamma_0 = ik_0\delta e^{-i\phi}/4C_{av}$ and $\gamma_1 = ik_1^2\delta e^{i\phi}/4k_z C_{av}$.

The up-conversion assumes the initial conditions of $v_0(0) = A_0$ and $v_1(0) = 0$, which gives

$$v_0(z) = A_0 \cos\left(\frac{\delta k_1}{4C_{av}} z\right), \quad (10a)$$

$$v_1(z) = A_0 \frac{k_1}{k_0} e^{+i\phi} \sin\left(\frac{\delta k_1}{4C_{av}} z\right). \quad (10b)$$

Equations (10a) and (10b) show that the change of the frequency and phase of the up-converted signal corresponds to the frequency and phase of the temporal modulation signal, Ω and $+\phi$. In addition, the maximum amplitude of the up-converted signal $a_1(z)$ occurs at $\delta k_1/C_{av} = 2\pi$. This reveals that, one can control the amplitude of the up-converted signal by changing the modulation amplitude δ . Following the same procedure, we can determine the input and output voltages for the down-conversion.

The down-conversion assumes the initial conditions of $v_0(0) = 0$ and $v_1(0) = A_1 = \text{Max}[v_1(z)] = A_0 k_1/k_0 \exp(+i\phi_0)$, which gives

$$v_1(z) = A_1 \cos\left(\frac{\delta k_1}{4C_{av}} z\right), \quad (11a)$$

and

$$v_0(z) = A_1 \frac{k_0}{k_1} e^{-i\phi} \sin\left(\frac{\delta k_1}{4C_{av}} z\right) = A_0 e^{i(\phi_0 - \phi)} \sin\left(\frac{\delta k_1}{4C_{av}} z\right). \quad (11b)$$

Equations (11a) and (11b) show that the change of the frequency and phase of the down-converted signal

corresponds to the frequency and phase of the temporal modulation signal, Ω and $-\phi$.

Figures 4(a) and 4(b) illustrate engineered frequency and phase transitions in the proposed temporal nonreciprocal phase shifter leading to opposite phase shifts for forward and backward signal transmissions. The structure is designed in a way to provide desired constructive and instructive interferences of different harmonics, and for both forward and backward signal transmissions. Two power splitters and combiners possessing two quarter-wavelength arms are utilized at two sides of the structure to attain the desired constructive and destructive interferences. In addition, a half-wavelength transmission line is placed at the middle of the structure to separate the two loops from each other and provide desired constructive and destructive interferences at different time harmonics. We aim to achieve a two-way complete signal transmission, but with opposite phase shifts for forward and backward transmissions, by proper engineering of the forward [Fig. 4(a)] and backward [Fig. 4(b)] frequency and phase

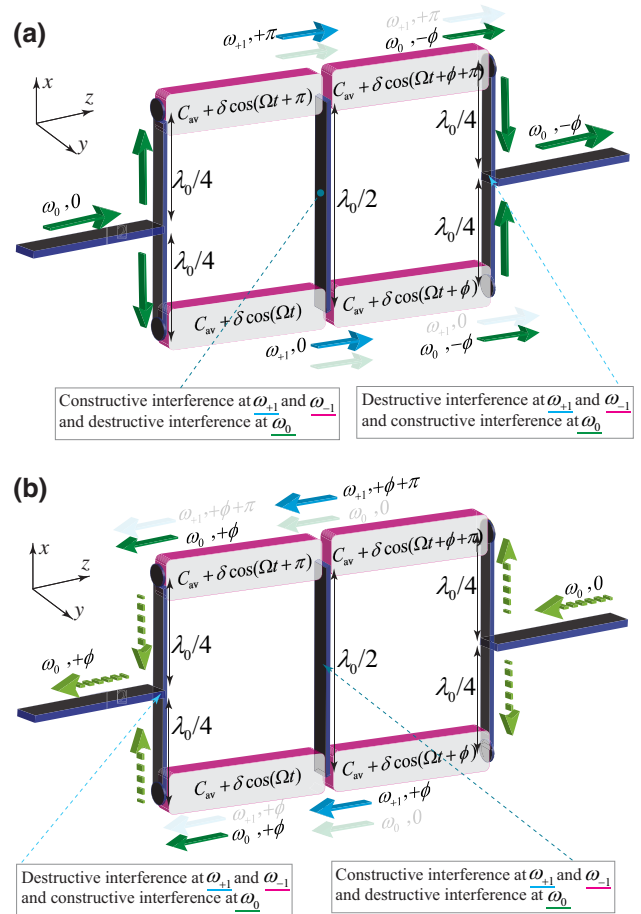


FIG. 4. Engineered frequency and phase transitions in the proposed temporal nonreciprocal phase shifter. (a) Forward signal injection. (b) Backward signal injection.

transitions in the proposed temporal nonreciprocal phase shifter.

Consider the forward signal injection in Fig. 4(a). The input signal is injected to the common port of the left power divider and flows in the upper and lower arms of the left loop. Next, these two signals make a transition to higher-order time harmonic ω_{+1} but with the $+\pi$ and 0 phase shifts in the upper and lower arms, respectively. Since the half-wavelength transmission middle interconnector makes a constructive interference at ω_{+1} , the generated ω_{+1} time harmonic reaches the right side loop. This leads to the generation of ω_0 harmonic by the right-side loop (second loop for the forward transmission), possessing identical phase shift of $-\phi$ in the upper and lower arms of the output of the right-side loop. As a consequence, since the power divider is formed by equal quarter-wavelength long arms, the signals add up at the common port of the right-side power divider. This yields a transmission at ω_0 with the phase shift of $-\phi$. We stress that, since the higher-order time harmonics $\omega_{+1} = \omega_0 + \Omega$ and $\omega_{-1} = \omega_0 - \Omega$ acquire a π -phase-shift difference at the two arms of the output (right) power divider, they will form a complete null at the output of the structure.

Now, consider the backward signal injection shown in Fig. 4(b). The input signal is injected to the common port of the right-side power divider and flows in the upper and lower arms of the right loop. Then, these two signals make a transition to higher-order time harmonic ω_{+1} but with the $+\phi + \pi$ and $+\phi$ phase shifts in the upper and lower arms, respectively. Similar to the forward signal transmission case, the half-wavelength transmission middle interconnector makes a constructive interference at ω_{+1} and a destructive interference at ω_0 . Hence, the generated ω_{+1} time harmonic reaches to the left-side loop. This leads to the generation of ω_0 harmonic by the left-side loop (second loop for the backward transmission), possessing identical phase shift of $+\phi$ in the upper and lower arms of the output of the right-side loop. As a result, since the power divider is formed by equal quarter-wavelength long arms, the signals add up at the common port of the left-side power combiner. This results in a transmission at ω_0 with the phase shift of $+\phi$, which is the opposite of the phase shift of the forward direction. Since the higher-order time harmonics ω_{+1} and ω_{-1} acquire a π -phase-shift difference at the two arms of the output (left) power divider, they will form a complete null at the output of the left power combiner. Such a contrast between the phase shift of the forward and backward transmissions originates from the asymmetric frequency-phase transitions in phase-engineered time-modulated structures.

As shown in Eq. (1), the nonreciprocal phase shifter of the proposed temporal circulator should introduce a forward phase shift of $\phi_{\text{NR}}^+ = \pi$ and a backward phase shift of $\phi_{\text{NR}}^- = 0$. Therefore, we design the nonreciprocal phase shifter of Fig. 4 for $\phi = \pi/2$ introducing forward

phase shift of $\phi^+ = \pi/2$ and backward phase shift of $\phi^- = -\pi/2$. Next, we connect each of the two arms of the nonreciprocal phase shifter to a $\lambda_g/8$ passive transmission line, where λ_g is the guided wavelength of the transmission line. Each of these two $\lambda_g/8$ passive transmission lines provide a reciprocal phase shift of $\pi/4$. As a consequence, the entire structure introduces a forward phase shift of $\phi_{\text{NR}}^+ = \pi/4 + \pi/2 + \pi/4 = \pi$, and a backward phase shift of $\phi_{\text{NR}}^- = \pi/4 - \pi/2 + \pi/4 = 0$.

III. EXPERIMENTAL DESIGN

Figure 5 shows an implementation of the time-modulated circulator by four phase-shifted time-varying varactors. Here, the two quarter-wavelength transmission lines on top of the figure form the two fixed reciprocal 90° phase shifters. The nonreciprocal phase shifter ($\phi_{\text{NR}}^+ = \pi$ and $\phi_{\text{NR}}^- = 0$) on the bottom of the structure is constituted of a nonreciprocal temporal phase shifter, with forward phase shift of $\phi^+ = \pi/2$ and backward phase shift of $\phi^- = -\pi/2$, and two $\lambda_g/8$ passive transmission-line-based phase shifters introducing a reciprocal phase shift of $\pi/4$ at each side of the nonreciprocal phase shifter. The nonreciprocal temporal phase shifter is constituted of the following components. Four varactors are used to create a phase-shifted time modulation. Two transmission-line-based power splitters feed the four temporal transmission lines, and the half-wavelength transmission line in the middle of the nonreciprocal temporal phase shifter provides constructive interference for the desired time harmonics and destructive interference for undesired time harmonics. Furthermore, four fixed inductors denoted by $L_{\text{chk}} = 390$ nH prevent leakage of the main microwave signal to the modulation line and phase shifters, eight fixed capacitances denoted by $C_{\text{cp}} = 10$ pF are considered for decoupling of the dc bias and low frequency modulation signal from the incident and transmitted high-frequency

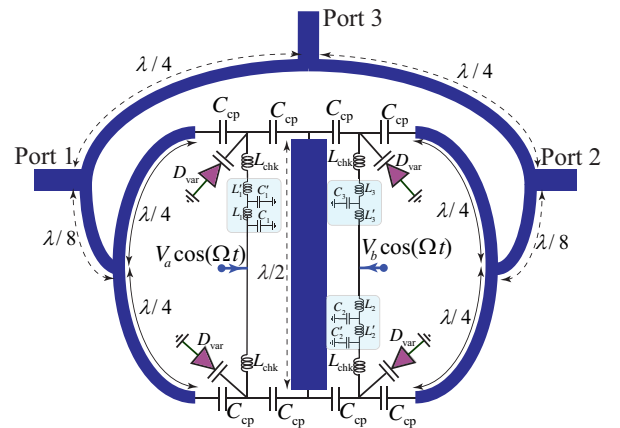


FIG. 5. Implementation of the time-modulated circulator by four phase-engineered time-varying varactors.

incident microwave signal. In addition, considering $\phi = 289^\circ$, the value of capacitances and inductances for three phase shifters in Fig. 5 read $C_1 = 16$ pF, $L_1 = 75$ nH, $C'_1 = 16$ pF, and $L'_1 = 57$ nH for 180° phase shift, and $C_2 = 16$ pF, $L_2 = 57$ nH, $C'_2 = 16$ pF, and $L'_2 = 75$ nH for 180° phase shift, and $C_3 = 10$ pF, $L_3 = 39$ nH, and $L'_3 = 39$ nH for 109° phase shift.

Figures 6(a) and 6(b) show the top and bottom views of the fabricated circulator, respectively. The circulator is designed at the center frequency of 4 GHz with the modulation frequency of $\Omega = 220$ MHz and modulation power of 15 dBm. Four SMV2019-079LF varactors manufactured by Skyworks Solutions Inc. are used for realizing the time modulation. We utilize a RT6010 substrate with permittivity $\epsilon_r = 10.2$, thickness $h = 1.27$ mm, and $\tan \delta = 0.0023$. Ports 1–3 are the main high frequency ports of the circulator (support 4 GHz), while two other ports at the bottom of the structure, i.e., Mod. 1 input and Mod. 2 input, support the low-frequency modulation signal injection with different phase shifts. The two 50-Ohm coplanar waveguide (CPW) transmission lines at the back of the structure, shown in Fig. 6(b), possess a width of $W = 1.143$ mm and a gap of $G = 0.508$ mm. In addition, the two $\lambda_g/8$ lines (shown in Fig. 5) are characterized by the width

$W = 0.635$ mm and length $l = 7.11$ mm, the two $\lambda_g/4$ lines (reciprocal phase shifters) on top of Fig. 5 possess the width $W = 0.635$ mm and length of $l = 14$ mm, the middle interconnector $\lambda_g/2$ line possesses the width of $W = 3.3$ mm and length of $l = 18.5$ mm, and the two $\lambda_g/4$ lines (power divider) inside the nonreciprocal phase shifter

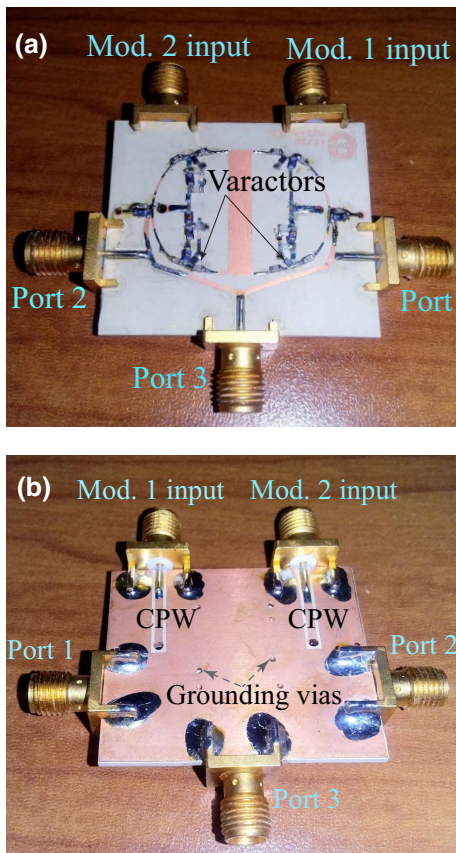


FIG. 6. Photo of the fabricated time-modulated circulator. (a) Top view. (b) Bottom view.

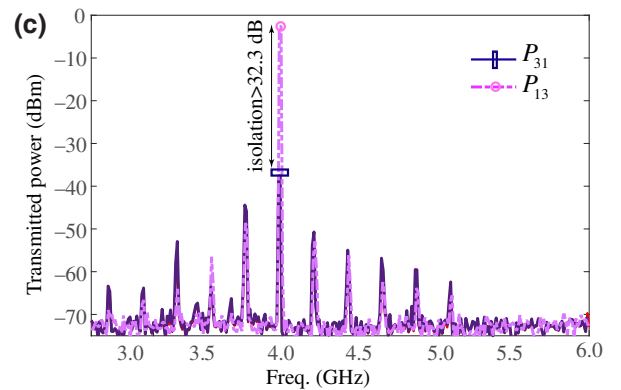
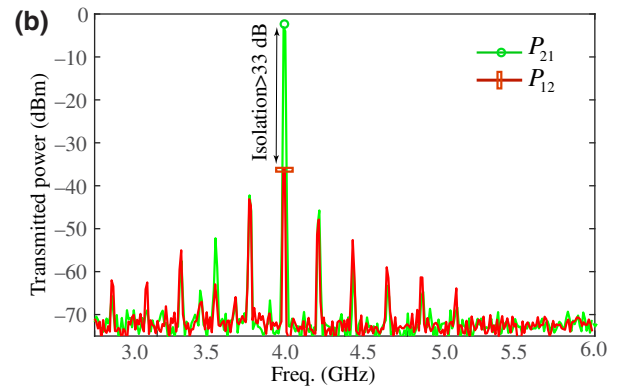
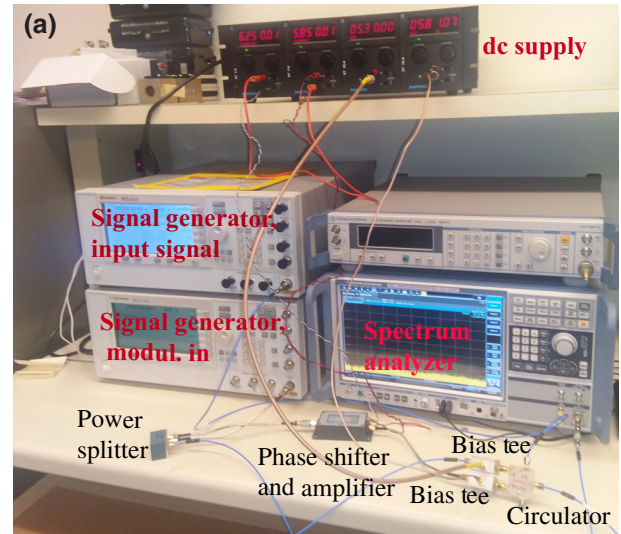


FIG. 7. Experimental results. (a) Photo of the measurement setup. (b) Power transmission from port 1 to port 2, P_{21} , and from port 2 to port 1, P_{12} . (c) Power transmission from port 1 to port 3, P_{31} , and from port 3 to port 1, P_{13} .

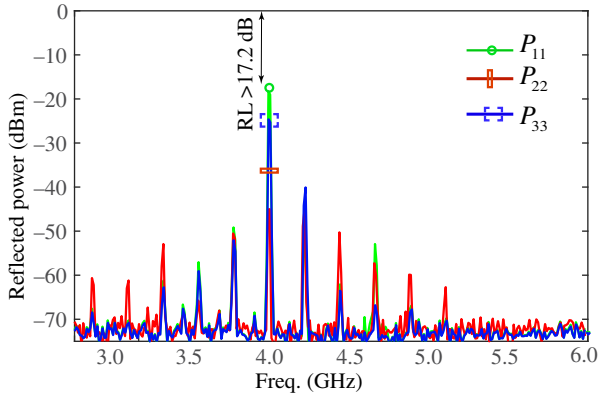


FIG. 8. Return loss (reflection) at three ports of the circulator, showing impedance matching at different ports.

are characterized by the width $W = 0.355$ mm and length $l = 18.5$ mm. We utilize two ZFBT-6GQ+ minicircuit bias tees to inject the modulation signals and dc biases to the varactors, concurrently.

Figure 7(a) shows a photo of the experimental setup for the measurement of the unidirectional signal transmission through the temporal circulator, where

$\Omega = 2\pi \times 220$ MHz. The measurement setup is formed by the device under test (temporal circulator), two Agilent E8257D signal generators, a FSW Rohde & Schwartz spectrum analyzer, a ZMSCJ-2 power splitter from Mini-Circuits, two ZFBT-6GW+ bias tees from Mini-Circuits, a phase shifter and amplifier providing the phase-engineered modulation signals, and a dc power supply chain that provides three independent dc sources. Figures 7(b) and 7(c) plot the experimental results for wave circulation between different ports of the circulator. It may be seen from the experimental results that an isolation of more than 32.3 dB between the ports is achieved, whereas the undesired time harmonics are highly suppressed, they are more than 40 dB lower than the main signals. Figure 8 plots the return loss (reflection) at three ports of the circulator, i.e., P_{11} , P_{22} , and P_{33} , where $P_{11} < 17.2$ dBm, $P_{22} < 35.3$ dBm, and $P_{33} < 22.4$ dBm. This figure shows that return loss (RL) of more than 17.2 dB is achieved at all ports of the circulator.

IV. DISCUSSION

Table I summarizes the performance of the fabricated circulator and provides a comparison between

TABLE I. Summary of the efficiency of the time-modulated circulator and comparison with previously reported circulators.

	Technology	Area	Freq. (GHz)	FBW (Isolation)	Isol. (dB)	IL (dB), IL ₂₁ /IL ₁₃	RL (dB)	P1dB (dBm)	IIP3 (dBm)
This work	Phase-engineered time modulation	$0.192\lambda^2$ (1080 mm ²)	4	22% (20 dB)	32.3	2.1/2.4	17.2	30.2	43.5
[56]	Ferrite magnets	$0.8\lambda^2$ (500 mm ²)	12	33.3% (10 dB)	10	1	10
[45]	Time-modulated resonators	$0.006\lambda^2$ (575 mm ²)	1	4% (20 dB)	55	3.3	10.8	29	33.7
[57]	Chip-space-time modulation	$0.0003\lambda^2$ (11.76 mm ²)	1.6	18% (25 dB)	25	2	> 10	10.5	...
[44]	Chip-space-time modulation across delay line	$0.015\lambda^2$ (2.16 mm ²)	25	18% (18.5 dB)	18.5	3.3/3.2	...	21.5	19.9
[58]	Chip-hybrid-coupler N-path	$0.000006\lambda^2$ (1mm ²)	0.725	27% (30 dB)	30	3.1/15	...	+5.5	14
[59]	Chip-switched TL gyrator	$0.0001\lambda^2$ (9mm ²)	1	18.4% (25 dB)	25	2.07/2.49	...	17.3	36.5
[60]	Chip-transistor (65-nm CMOS), Δ resonators	$0.023\lambda^2$ (0.21 mm ²)	100	1.5% (45 dB)	46	5.6	> 10	11.4	...
[61]	Chip-transistor (180-nm CMOS), Feedforward	$0.021\lambda^2$ (3.22 mm ²)	24	1% (15 dB)	20	-12.3/ - 22.4 (gain)	> 8	-19.8	-11
[62]	Chip-transistor (180-nm CMOS), Current reuse	$0.0036\lambda^2$ (0.36 mm ²)	30	7.6% (15 dB)	12	7.5/5	> 6	-7	...
[63]	Chip-transistor (180-nm CMOS), Cancellation	$0.0022\lambda^2$ (0.35mm ²)	24	11.2% (15 dB)	30	8.5/9	> 8.5	-12	...
[64]	Chip-transistor (90-nm CMOS), Amps	$0.01\lambda^2$ (0.93mm ²)	31.75	58% (15 dB)	12 ~ 22	9/3.5	> 3	-3	...
[65]	Chip-transistor (180-nm CMOS), isolators	$0.004\lambda^2$ (0.715 mm ²)	24	3% (15 dB)	20	5.7/5.7	> 16	9.5	...

the performance of this circulator and that of recently proposed circulators with different techniques, including space-time (ST) modulation, magnetic-ferrite-loaded waveguides, nonlinearity, and transistor-loaded transmission lines. In this table, IL stands for insertion loss, RL stands for return loss, and FBW is an acronym for the fractional bandwidth, which is equal to the frequency bandwidth over the center frequency. Additionally, P1dB is the output 1-dB compression point, which shows the prominent linearity of the circulator. Additionally, IIP3 represents the third-order intercept point, which is a hypothetical point where the power levels of the third-order components and the fundamental component meet each other. Calculating the IIP3 is a method of quantifying intermodulation distortion and determining the linearity of the circulator. A high IIP3 value demonstrates outstanding linearity of the circulator, while low IIP3 value shows that the intermodulation products could interfere with the fundamental signal.

The proposed circulator can be realized in a much more compact fashion, and may be integrated into chip technology for high frequencies thanks to the availability of variable capacitors at high frequencies [42]. In addition, in contrast to the transistor-based circulator [50] where nonlinear and low-power handling transistors are placed in series with the incident signal, our circulator is endowed by high-power rating as the varactors are placed in parallel to the incident signal. In our experiment, we apply up to +33-dBm input signal, and the power rating is expected to exceed 47 dBm. Having leveraged the linear properties of the time modulation, the proposed temporal circulator exhibits an outstanding linear response, where the P1dB is +30.2 dBm and IIP3 is +43.5 dBm.

The frequency bandwidth of this temporal circulator can be enhanced by using engineering approaches for the bandwidth enhancement of power splitters, e.g., using nonuniform transmission lines and transmission lines [51,52], and broad-band phase shifters [53–55]. Additionally, voltage-controlled varactor-based phase shifters may be utilized to enhance performance and controllability of the circulator.

V. CONCLUSION

In summary, we propose a lightweight compact nonmagnetic time-varying circulator. The circulator is based on a time-modulated nonreciprocal phase shifter. The proposed nonreciprocal phase shifter exhibits great performance including nonreciprocal phase-shift range, and can be adopted for broad-band operation. The experimental results demonstrate a strong isolation level of more than 32.3 dB, which can be further improved. Furthermore, the unwanted time harmonics are 40 dB lower than the main signal. What is more, this circulator exhibits a highly linear response, with the P1dB of +30.2 dBm and the IIP3 of 43.5 dBm. Such promising results and compact

profile of the circulator can be further improved and optimized in future work. Furthermore, the proposed structure can be redesigned for integration into integrated circuit technology to achieve much smaller profile and versatile operation.

ACKNOWLEDGMENTS

This work is supported by the Natural Sciences and Engineering Research Council of Canada (NSERC).

-
- [1] Edward A. Ohm, A broad-band microwave circulator, *IRE Trans. Microw. Theory Tech.* **4**, 210 (1956).
 - [2] A. K. Kamal, A parametric device as a nonreciprocal element, *Proc. IRE* **48**, 1424 (1960).
 - [3] C. E. Fay and R. L. Comstock, Operation of the ferrite junction circulator, *IEEE Trans. Microw. Theory Tech.* **13**, 15 (1965).
 - [4] Douglas K. Linkhart, *Microwave Circulator Design* (Artech House, Norwood, MA, 2014).
 - [5] Ahmed Kord, Dimitrios L. Sounas, and Andrea Alu, Microwave nonreciprocity, *Proc. IEEE* **108**, 1728 (2020).
 - [6] Sajjad Taravati and George V. Eleftheriades, in *2021 IEEE MTT-S International Microwave Symposium (IMS)* (IEEE, Atlanta, GA, 2021), p. 412.
 - [7] S. D. Ewing and J. E. R. A. L. D. A. Weiss, Ring circulator theory, design, and performance, *IEEE Trans. Microw. Theory Tech.* **15**, 623 (1967).
 - [8] Benton K. O’Neil and Jeffrey L. Young, Experimental investigation of a self-biased microstrip circulator, *IEEE Trans. Microw. Theory Tech.* **57**, 1669 (2009).
 - [9] Fei Fan, Sheng-Jiang Chang, Chao Niu, Yu Hou, and Xiang-Hui Wang, Magnetically tunable silicon-ferrite photonic crystals for terahertz circulator, *Opt. Commun.* **285**, 3763 (2012).
 - [10] S. Tanaka, N. Shimomura, and K. Ohtake, Active circulators: The realization of circulators using transistors, *Proc. IEEE* **53**, 260 (1965).
 - [11] Mark A. Smith, in *Microw. Sympos. Digest, 1988.*, *IEEE MTT-S Int.* (IEEE, New York, 1988), p. 1015.
 - [12] Yalcin Ayasli, Field effect transistor circulators, *IEEE Trans. Magn.* **25**, 3242 (1989).
 - [13] Christos Kallialakis, Martin J. Cryan, Peter S. Hall, and Peter Gardner, Analysis and design of integrated active circulator antennas, *IEEE Trans. Microw. Theory Tech.* **48**, 1017 (2000).
 - [14] Geert Carchon and B. Nanwelaers, Power and noise limitations of active circulators, *IEEE Trans. Microw. Theory Tech.* **48**, 316 (2000).
 - [15] Sajjad Taravati and George V. Eleftheriades, Programmable nonreciprocal meta-prism, *Sci. Rep.* **11**, 1 (2021).
 - [16] George V. Eleftheriades and Sajjad Taravati, Full-duplex reflective beamsteering metasurface featuring magnetless nonreciprocal amplification, *Nat. Commun.* **14**, 4414 (2021).
 - [17] Suhas Bhandare, Selwan K. Ibrahim, David Sandel, Hongbin Zhang, F. Wust, and Reinhold Noé, Novel nonmagnetic 30-dB traveling-wave single-sideband optical isolator

- integrated in III/V material, *IEEE J. Sel. Top. Quantum Electron.* **11**, 417 (2005).
- [18] Zongfu Yu and Shanhui Fan, Complete optical isolation created by indirect interband photonic transitions, *Nat. Photonics* **3**, 91 (2009).
- [19] Sajjad Taravati and Ahmed A. Kishk, Space-time modulation: Principles and applications, *IEEE Microw. Mag.* **21**, 30 (2020).
- [20] Miguel Camacho, Brian Edwards, and Nader Engheta, Achieving asymmetry and trapping in diffusion with spatiotemporal metamaterials, *Nat. Commun.* **11**, 1 (2020).
- [21] Sajjad Taravati, Nima Chamanara, and Christophe Caloz, Nonreciprocal electromagnetic scattering from a periodically space-time modulated slab and application to a quasisonic isolator, *Phys. Rev. B* **96**, 165144 (2017).
- [22] Sajjad Taravati, Self-biased broadband magnet-free linear isolator based on one-way space-time coherency, *Phys. Rev. B* **96**, 235150 (2017).
- [23] Junfei Li, Chen Shen, Xiaohui Zhu, Yangbo Xie, and Steven A. Cummer, Nonreciprocal sound propagation in space-time modulated media, *Phys. Rev. B* **99**, 144311 (2019).
- [24] Sajjad Taravati, Giant Linear Nonreciprocity, Zero Reflection, and Zero Band Gap in Equilibrated Space-Time-Varying Media, *Phys. Rev. Appl.* **9**, 064012 (2018).
- [25] Sajjad Taravati and George V. Eleftheriades, Generalized Space-Time Periodic Diffraction Gratings: Theory and Applications, *Phys. Rev. Appl.* **12**, 024026 (2019).
- [26] Sajjad Taravati and George V. Eleftheriades, Lightweight low-noise linear isolator integrating phase-and amplitude-engineered temporal loops, *Adv. Mat. Technol.* **7**, 2100674 (2021).
- [27] P. K. Tien and H. Suhl, A traveling-wave ferromagnetic amplifier, *Proc. IEEE* **46**, 700 (1958).
- [28] P. K. Tien, Parametric amplification and frequency mixing in propagating circuits, *J. Appl. Phys.* **29**, 1347 (1958).
- [29] Xiaohui Zhu, Junfei Li, Chen Shen, Guangyu Zhang, Steven A. Cummer, and Longqiu Li, Tunable unidirectional compact acoustic amplifier via space-time modulated membranes, *Phys. Rev. B* **102**, 024309 (2020).
- [30] Sajjad Taravati and Ahmed A. Kishk, Dynamic modulation yields one-way beam splitting, *Phys. Rev. B* **99**, 075101 (2019).
- [31] Sajjad Taravati, Aperiodic space-time modulation for pure frequency mixing, *Phys. Rev. B* **97**, 115131 (2018).
- [32] Sajjad Taravati and George V. Eleftheriades, Pure and Linear Frequency-Conversion Temporal Metasurface, *Phys. Rev. Appl.* **15**, 064011 (2021).
- [33] Joachim Werner Zang, Diego Correas-Serrano, J. T. S. Do, Xiaoguang Liu, Alejandro Alvarez-Melcon, and Juan Sebastian Gomez-Diaz, Nonreciprocal Wavefront Engineering with Time-Modulated Gradient Metasurfaces, *Phys. Rev. Appl.* **11**, 054054 (2019).
- [34] Sajjad Taravati and Ahmed A. Kishk, Advanced wave engineering via obliquely illuminated space-time-modulated slab, *IEEE Trans. Antennas Propag.* **67**, 270 (2019).
- [35] Sajjad Taravati and George V. Eleftheriades, 4D wave transformations enabled by space-time metasurfaces: Foundations and illustrative examples, *IEEE Antennas Propag. Mag.*, 2 (2022).
- [36] Sajjad Taravati and George V. Eleftheriades, Microwave space-time-modulated metasurfaces, *ACS Photonics* **9**, 305 (2022).
- [37] J. W. Zang, A. Alvarez-Melcon, and J. S. Gomez-Diaz, Nonreciprocal Phased-Array Antennas, *Phys. Rev. Appl.* **12**, 054008 (2019).
- [38] Xiaohu Wu, Mahmoud Nafe, Alejandro Álvarez Melcón, Juan Sebastián Gómez-Díaz, and Xiaoguang Liu, Frequency tunable non-reciprocal bandpass filter using time-modulated microstrip $\lambda_g/2$ resonators, *IEEE Trans. Circ. Syst. II: Express Briefs* **68**, 667 (2020).
- [39] Sajjad Taravati and Christophe Caloz, Mixer-duplexer-antenna leaky-wave system based on periodic space-time modulation, *IEEE Trans. Antennas Propag.* **65**, 442 (2017).
- [40] Sajjad Taravati and George V. Eleftheriades, Space-Time Medium Functions as a Perfect Antenna-Mixer-Amplifier Transceiver, *Phys. Rev. Appl.* **14**, 054017 (2020).
- [41] Xinpeng Huang and Shanhui Fan, Complete all-optical silica fiber isolator via stimulated Brillouin scattering, *J. Lightwave Technol.* **29**, 2267 (2011).
- [42] Hugo Lira, Zongfu Yu, Shanhui Fan, and Michal Lipson, Electrically Driven Nonreciprocity Induced by Interband Photonic Transition on a Silicon Chip, *Phys. Rev. Lett.* **109**, 033901 (2012).
- [43] Nicholas A. Estep, Dimitrios L. Sounas, Jason Soric, and Andrea Alù, Magnetic-free non-reciprocity and isolation based on parametrically modulated coupled-resonator loops, *Nat. Phys.* **10**, 923 (2014).
- [44] Tolga Dinc, Aravind Nagulu, and Harish Krishnaswamy, A millimeter-wave non-magnetic passive SOI CMOS circulator based on spatio-temporal conductivity modulation, *IEEE J. Solid-State Circuits* **52**, 3276 (2017).
- [45] Ahmed Kord, Dimitrios L. Sounas, and Andrea Alù, Magnet-less circulators based on spatiotemporal modulation of bandstop filters in a delta topology, *IEEE Trans. Microw. Theory Tech.* **66**, 911 (2017).
- [46] Aravind Nagulu, Tolga Dinc, Zhicheng Xiao, Mykhailo Tymchenko, Dimitrios L. Sounas, Andrea Alù, and Harish Krishnaswamy, Nonreciprocal components based on switched transmission lines, *IEEE Trans. Microw. Theory Tech.* **66**, 4706 (2018).
- [47] Haysam M. Kadry, Mohammad Alhawari, and Dimitrios L. Sounas, Angular-momentum biased circulator with locally generated modulation, *IEEE Trans. Microw. Theory Tech.* **69**, 551 (2020).
- [48] Sajjad Taravati and George V. Eleftheriades, Full-Duplex Nonreciprocal Beam Steering by Time-Modulated Phase-Gradient Metasurfaces, *Phys. Rev. Appl.* **14**, 014027 (2020).
- [49] Peter Halevi, Jorge R. Zurita-Sánchez, and Juan C. Cervantes-González, Reflection and transmission of a wave incident on a slab with a time-periodic dielectric function $\epsilon(t)$, *Phys. Rev. A* **79**, 053821 (2009).
- [50] S. Tanaka, N. Shimomura, and K. Ohtake, Active circulators—the realization of circulators using transistors, *Proc. IEEE* **53**, 260 (1965).
- [51] S. Taravati and M. Khalaj-Amirhosseini, Generalised single-section broad-band asymmetrical Wilkinson power divider, *IET Microw. Antennas Propag.* **6**, 1164 (2012).
- [52] Sajjad Taravati and Mohammad Khalaj-Amirhosseini, An efficient method of designing dual- and wide-band power

- dividers with arbitrary power division, *Int. J. RF Microw. Comput.-Aided Eng.* **23**, 118 (2013).
- [53] Tang Xinyi, in *Huazhong University of Science and Technology* (National University of Singapore, China, 2011).
- [54] Sajjad Taravati, Shulabh Gupta, Qingfeng Zhang, and Christophe Caloz, Enhanced bandwidth and diversity in real-time analog signal processing (R-ASP) using nonuniform c-section phasers, *IEEE Microw. Wireless Compon. Lett.* **26**, 663 (2016).
- [55] Ryota Komaru, Masatake Hangai, Shintaro Shinjo, and Takuo Morimoto, in *2019 49th European Microwave Conference (EuMC)* (IEEE, Paris, 2019), p. 836.
- [56] Leticia Martinez, Vincent Laur, Alejandro L. Borja, Patrick Quéffélec, and Angel Belenguer, Low loss ferrite Y-junction circulator based on empty substrate integrated coaxial line at Ku-band, *IEEE Access* **7**, 104789 (2019).
- [57] Shihan Qin and Yuanxun Ethan Wang, in *2016 IEEE MTT-S International Microwave Symposium (IMS)* (IEEE, 2016), p. 1.
- [58] Sanket Jain, Abhishek Agrawal, Manoj Johnson, and Arun Natarajan, in *2018 IEEE International Solid-State Circuits Conference-(ISSCC)* (IEEE, San Francisco, 2018), p. 400.
- [59] Aravind Nagulu, Tingjun Chen, Gil Zussman, and Harish Krishnaswamy, Multi-Watt, 1-GHz CMOS circulator based on switched-capacitor clock boosting, *IEEE J. Solid-State Circuits* **55**, 3308 (2020).
- [60] Chang Yang and Ping Gui, 85–110-GHz CMOS magnetic-free nonreciprocal components for full-duplex transceivers, *IEEE J. Solid-State Circuits* **54**, 368 (2018).
- [61] Hsien-Shun Wu, Chao-Wei Wang, and Ching-Kuang Clive Tzuang, CMOS active quasi-circulator with dual transmission gains incorporating feedforward technique at K-band, *IEEE Trans. Microw. Theory Tech.* **58**, 2084 (2010).
- [62] Chia-Hao Chang, Yu-Tsung Lo, and Jean-Fu Kiang, A 30 GHz active quasi-circulator with current-reuse technique in 0.18- μm CMOS technology, *IEEE Microw. Wireless Compon. Lett.* **20**, 693 (2010).
- [63] Ding-Jie Huang, Jing-Lin Kuo, and Huei Wang, in *2012 IEEE/MTT-S International Microwave Symposium Digest* (IEEE, Montreal, 2012), p. 1.
- [64] Shih-Han Hung, Kai-Wen Cheng, and Yeong-Her Wang, An ultra wideband quasi-circulator with distributed amplifiers using 90 nm CMOS technology, *IEEE Microw. Wireless Compon. Lett.* **23**, 656 (2013).
- [65] Jen-Feng Chang, Jui-Chih Kao, Yu-Hsuan Lin, and Huei Wang, Design and analysis of 24-GHz active isolator and quasi-circulator, *IEEE Trans. Microw. Theory Tech.* **63**, 2638 (2015).